Inorganic Chemistry

Article

pubs.acs.org/IC

Control of TiO_2 Grain Size and Positioning in Three-Dimensionally Ordered Macroporous TiO_2/C Composite Anodes for Lithium Ion Batteries

Nicholas D. Petkovich,[†] Stephen G. Rudisill,[†] Benjamin E. Wilson,[†] Anwesha Mukherjee,[‡] and Andreas Stein*,[†]

[†]Department of Chemistry, University of Minnesota, 207 Pleasant Street SE, Minneapolis, Minnesota 55455, United States

[‡]Department of Chemistry, Indian Institute of Technology Guwahati, Guwahati 781039, Assam, India

Supporting Information

ABSTRACT: After several high-profile incidents that raised concerns about the hazards posed by lithium ion batteries, research has accelerated in the development of safer electrodes and electrolytes. One anode material, titanium dioxide (TiO_2), offers a distinct safety advantage in comparison to commercialized graphite anodes, since TiO_2 has a higher potential for lithium intercalation. In this article, we present two routes for the facile, robust synthesis of nanostructured TiO_2/carbon composites for use as lithium ion battery anodes. These materials are made using a combination of colloidal crystal templating and surfactant templating, leading to the first report of a three-dimensionally ordered macroporous TiO_2/C composite with mesoporous walls. Control over the size and location of the TiO_2 crystallites in the composite (an often difficult task) has been achieved by changing the chelating agent in the precursor. Adjustment of the pyrolysis temperature has also allowed us to strike a balance between the size of the TiO_2 crystallites and the degree of carbonization. Using these pathways to optimize electrochemical performance, the primarily macroporous TiO_2/C composites can attain a capacity of 171 mAh/g at a rate of 1 C. Additionally, the carbon in these composites can function as a secondary template for high-surface-area, macroporous TiO_2 with disordered mesoporous voids. Combining the advantages of a nanocrystalline framework and significant open porosity, the macroporous TiO_2 delivers a stable capacity (>170 mAh/g at a rate of C/2) over 100 cycles.

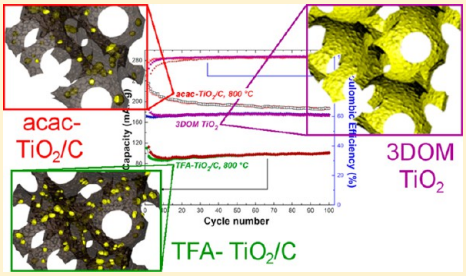

INTRODUCTION

Titanium is the second most abundant transition metal in the Earth's crust, and its oxide, TiO_2, finds use in a wide array of applications. Since TiO_2 is a wide band gap semiconductor, its electronic properties have been harnessed for photocatalysis,[1,2] electronic device fabrication,[3,4] and the creation of dye-sensitized solar cells.[5,6] TiO_2 also serves as an important component in many pigments[7] and in stable supports for catalytic materials.[8−10] While many of these applications for TiO_2 have been developed over decades, the emergence of TiO_2 as a material for lithium ion battery anodes has happened only recently.[10] Despite limitations inherent to TiO_2, researchers have begun to utilize TiO_2 effectively in batteries. Some of the benefits of using TiO_2 are clear, e.g. its cost, low toxicity, and density, while others were discovered through the electrochemical testing of TiO_2. In many cases, these benefits can only be realized when modifications are made to the various polymorphs of TiO_2, as described below.

Huang et al. first reported on the use of anatase TiO_2 as an intercalation-based anode material that could potentially compete with graphite-based anodes used in lithium ion batteries.[11] As research into the electrochemistry of TiO_2 progressed from that point, two advantages of using TiO_2 were touted.[12−14] First, the lithium intercalation and deintercalation processes in TiO_2 take place at a higher voltage than in graphite (~1.4 to 1.8 V vs Li^+/Li, depending on the polymorph).[10] While this operating potential does not necessarily eliminate irreversible capacity due to formation of the solid−electrolyte interphase,[15] it avoids the problems of lithium plating and dendrite formation. With continued concerns over lithium ion battery safety, especially in light of recent incidents in the transportation sector, this advantage is especially relevant.[16] Another key advantage of TiO_2 is that it can retain its capacity at fast charge/discharge rates, but only in TiO_2 materials with nanoscale features, not in their bulk counterparts.[17−20] Careful control of the overall morphology of TiO_2 is needed to obtain good rate performance and to obtain reasonable capacities that make TiO_2 competitive with graphite.[10,20]

The past decade of research into TiO_2 electrodes has been marked by a continued push to synthesize materials that can deliver good capacities at high rates. These efforts have focused on the synthesis of nanoporous TiO_2,[21−23] TiO_2 particles with extremely small crystallite sizes,[18,24,25] and intricate hierarchical structures of TiO_2.[26,27] Most of these engineered materials

Received: October 21, 2013
Published: January 6, 2014

   dx.doi.org/10.1021/ic402648f | Inorg. Chem. 2014, 53, 1100−1112

possess high surface areas and have an open morphology that allows the electrolyte to completely wet the active material. As a result of these morphologies, lithium ion diffusion distances are reduced and a large interfacial area can be utilized for insertion/extraction reactions. In addition, the extensive interface between the active material and the electrolyte helps contribute to pseudocapacitance charge storage.[22,28] Pseudocapacitance becomes the dominant reversible charge storage mechanism for TiO_2 at high charge/discharge rates.[22] Significant reductions in the crystallite size of TiO_2 also assist in increasing the extent of lithium intercalation, leading to improvements in capacity.[22,29]

Moving beyond simply considering the morphology of pure TiO_2, substantial research has been performed on composite materials that contain TiO_2 and a secondary conductive phase. As a wide band gap semiconductor, TiO_2 has low intrinsic electronic conductivity. The low electronic conductivity of TiO_2 can significantly reduce battery capacities at high rates when electron transport lengths are relatively long, as is the case for nanoporous materials that extend over micrometers in length. This limitation is overcome through doping with heteroatoms[30] or though the formation of composite materials.[10] Most TiO_2 electrodes are fairly "low-tech" composites, in which TiO_2 is mechanically mixed with a conductive additive, typically carbon black. Better "wiring" of the TiO_2 grains can be realized through the formation of a nanocomposite, wherein the active TiO_2 is intimately mixed with the conductive phase during materials synthesis.[31] Guo et al. accomplished this by using sol–gel-derived RuO_2 "wires" with a matrix of TiO_2 crystals.[32] Owing to the expense of RuO_2, other groups have focused on forming nanocomposites with conductive carbon allotropes. Various composites have been produced that exhibit a wide range of morphologies that are often determined by the type of carbon used. For instance, TiO_2 nanosheets have been grown on carbon nanotubes that easily transport electrons away from the sheets, thereby improving performance at fast charge/discharge rates.[33] The use of graphene in nanocomposites with TiO_2 has allowed for the generation of different morphologies. Graphene can be used to wrap TiO_2 crystallites in a conductive matrix[34,35] and has also been used to produce sandwichlike composites with TiO_2 sheets.[36] Amorphous carbon is another allotrope that can be combined with TiO_2 in a variety of syntheses.[37−40] Its versatility comes in part from the numerous compounds that can be pyrolyzed to form a conductive phase, and one such compound is critical in the study described herein.

This article describes an effort to improve the performance of TiO_2 for lithium ion battery anodes through the formation of nanostructured TiO_2/C composites. In addition, it explores the use of the carbon as a secondary template to minimize TiO_2 crystallite growth during thermal processing. To obtain a suitable morphology, a combination of colloidal crystal templating (CCT) and surfactant templating is employed. This technique has been proven to produce hierarchical materials with an interconnected face-centered-cubic (fcc) lattice of macropores (via removal of the colloidal crystal) and with a mesopore network in the wall (via removal of the surfactant).[41] The synthesis of materials with this morphology—known as a three-dimensionally ordered macroporous structure with mesoporous walls (3DOM/m structure)—is generally accomplished through infiltration of a liquid precursor into the void spaces of a colloidal crystal. For preparation of the TiO_2/C composites discussed here, a multiconstituent precursor is used that contains titanium isopropoxide (TiO_2 source), a phenol–formaldehyde (PF) sol (amorphous carbon source), and a block copolymeric surfactant. Further processing at elevated temperatures removes the colloidal crystal template, crystallizes the TiO_2, and carbonizes the PF sol. Ultimately, a porous structure is formed that contains nanocrystals of TiO_2 in a conductive carbon matrix, allowing better utilization of TiO_2 as an anode material.

We have discovered that specific alterations to the synthesis procedure have a significant impact on the performance of these materials as lithium ion battery anodes. First, both the choice of chelating agent and the temperature used for pyrolysis influence the TiO_2 crystallite size. This translates into significant differences in the performance of the TiO_2/C composites. Second, removal of the carbon framework through combustion at low temperatures yields a three-dimensionally ordered macroporous (3DOM) TiO_2 with void spaces between crystallites. The carbon restricts TiO_2 crystallite growth prior to burnout and allows us to achieve good capacities with this particular material.

EXPERIMENTAL SECTION

Materials. Methyl methacrylate (99%), titanium(IV) isopropoxide (>97%), 2,4-pentadione (acac, 99+%), trifluoroacetic acid (TFA, 99%), poly(ethylene oxide)–*block*-poly(propylene oxide)–*block*-poly(ethylene oxide) copolymer (molecular weight of 5800, P123), and sodium carboxymethyl cellulose (molecular weight of 250000) were all purchased from Sigma-Aldrich. Phenol (ACS reagent grade), formaldehyde (37 wt % in water), and potassium persulfate (ACS reagent grade) were obtained from Fisher Scientific. Hydrochloric acid (37 wt % in water) and sodium hydroxide pellets (ACS reagent grade) were obtained from Macron Chemicals. A suspension of styrene–butadiene rubber (50 wt % in water) was purchased from the MTI Corp. Ethanol (200 proof, USP grade) was purchased from Decon Laboratories. Aeroxide P25 TiO_2 was provided by Evonik Industries. All chemicals were used without further purification. Deionized water was produced on site using a Barnstead Sybron purification system (final resistivity >18 MΩ cm).

Preparation of the TFA-TiO_2/C Composites. To produce these materials, monodisperse colloidal spheres of poly(methyl methacrylate) (PMMA) were synthesized using a previously reported emulsifier-free emulsion polymerization.[42] Colloidal crystal templates were obtained by letting the sphere suspension sediment under the force of gravity and then by allowing the supernatant to evaporate. Phenol–formaldehyde prepolymer sol was synthesized following a well-established literature procedure.[43] The final sol was produced by dispersing dried resol oligomers in an equal mass of ethanol, forming a 50 wt % ethanolic PF sol. After the PF sol was obtained, two separate solutions (solutions A and B) were made. In solution A, 3.5 g of titanium isopropoxide was mixed with 1.4 g of TFA. This solution was stirred, and 2 g of ethanol was then added. After 5 min of stirring, 0.6 g of concentrated HCl was added dropwise to it. P123 (0.75 g), gently heated to a liquid state, was then added to the solution. Solution A was stirred until complete dissolution of the P123 was achieved. In solution B, 0.3 g of PF sol was mixed with 2 g of ethanol. Water (0.88 g) and liquid P123 (1 g) were added to solution B. Solution B was stirred until the P123 completely dissolved. Once the P123 had dissolved in both solutions, solution B was added dropwise to solution A. The final precursor solution was stirred overnight.

For infiltration, millimeter-sized monolithic colloidal crystal templates were first placed in 20 mL scintillation vials. The precursor solution was then injected into the vials up to half the height of the template monoliths. Capillary action drew the precursor into the templates over a period of 4–6 h. If all the precursor solution was taken up into the templates, a small amount of additional precursor was added to the vials. After infiltration was completed, excess precursor was wiped from the monoliths using laboratory wipes. Excess solvent was removed by placing the infiltrated templates under

dx.doi.org/10.1021/ic402648f | Inorg. Chem. 2014, 53, 1100−1112

low vacuum at ambient temperature for 15 min. This was done to prevent destruction of the 3DOM structure during subsequent pyrolysis. The infiltrated monoliths were then thermally treated (in capped vials) at 100 °C for 24 h and then at 140 °C for 24 h to further condense and cross-link the components of the precursor. They were then placed in alumina boats in a quartz tube under Ar gas flow (0.7 L/min) to remove the template, crystallize the TiO_2, and carbonize the PF resin. Samples were heated in a tube furnace to 350 °C at 1 °C/min and held for 4 h and then to 500, 600, 700, 800, or 900 °C at 1 °C/min and held for 2 h.

Preparation of Pure 3DOM TiO_2. For the pure 3DOM TiO_2, a TFA-based composite was first prepared. Pyrolysis was conducted at 350 and 500 °C following the procedure detailed above. Carbon was removed from the composites by calcining them at 400 °C for 2 h in a tube furnace under static air. A ramp rate of 2 °C/min was used.

Preparation of the acac-TiO_2/C Composites. A similar procedure to the one described above was used for the precursor solutions that contained acac as a chelating agent. Once again, a 50 wt % PF sol in ethanol was used for this synthesis. Two solutions (A and B) were prepared. Solution A was made by first combining 3.5 g of titanium isopropoxide with 1.23 g of acac. Shortly after these were mixed, 1.75 g of ethanol was added to solution A. After 5 min of stirring, 1 g of concentrated HCl was added dropwise while solution A was stirred. Liquid P123 (0.75 g) was then dissolved in solution A. For solution B, ethanol (1.75 g) and PF sol (0.27 g) were mixed. Subsequently, 0.75 g of water and 1 g of liquid P123 was added to the solution. Once P123 had dissolved in both solutions A and B, solution B was added dropwise to solution A. The final precursor was stirred overnight. Infiltration of the colloidal crystal templates and subsequent processing was conducted following the procedure detailed above for the TFA–TiO_2/C composites.

Product Characterization. All of the samples were characterized by powder X-ray diffraction (PXRD) using a PANalytical X'Pert PRO diffractometer operated with a Co anode at 45 kV and 40 mA and an X'Celerator detector. The Scherrer equation was used to estimate crystallite sizes via line broadening in the PXRD patterns. Further characterization of the crystal structures present in the samples was performed using a WITec Alpha300R confocal Raman microscope fitted with a 514.5 nm Ar^+ laser (operated at 15 mW). Raman scattering was detected using a DV401 CCD thermoelectric-cooled detector. Multiple spectra were collected for a given area and then averaged to give the final, reported spectrum. A 10× aperture was used for all measurements. Morphological information was obtained via scanning electron microscopy (SEM) performed with a JEOL 6700 instrument operated at 5 kV. Samples were mounted on Al stubs covered with double-sided sticky carbon tape. A 5 nm layer of Pt was deposited on the samples prior to imaging. Additional morphological information was obtained by transmission electron microscopy (TEM). An FEI Technai T12 operated at 120 kV with LaB_6 filament was used for TEM imaging. Samples were prepared by bath sonicating powders suspended in ethanol for 5 min. The suspensions were dropped onto Cu grids coated with Formvar. Small-angle X-ray scattering (SAXS) patterns were collected on a Rigaku RU-200BVH instrument equipped with a rotating copper anode and a Siemens Hi-Star multiwire area detector. Gas sorption isotherms were obtained using a Quantachrome Autosorb IQ_2 with N_2 gas at 77 K. Samples were outgassed at 200 °C and 0.001 Torr for 12 h prior to measurement. Surface areas were calculated using the Brunauer–Emmitt–Teller (BET) method. Pore volumes were calculated from the point $P/P_0 = 0.995$ on the adsorption branch. Micropore volumes were estimated using a quenched solid density functional theory (QSDFT) kernel supplied by Quantachrome Instruments. Thermogravimetric analysis was conducted using a Netzsch STA 409 PC Luxx instrument to determine the TiO_2 content. Analyses were carried out in flowing air using a 10 °C/min ramp up to 1000 °C. Fluorine content in the TFA composite samples was determined via a combination of flask combustion and ion chromatography carried out by Atlantic Microlab (Norcross, GA).

Electrochemical Characterization. Electrodes were assembled by mixing ground, ultrasonicated active material, Timcal Super P carbon black, and the aqueous binder suspensions. This electrode paste was spread onto carbon-coated aluminum foil (provided by Exopack Advanced Coatings) and dried overnight at room temperature and finally under vacuum at 105 °C for 24 h. The composition of the dried electrode film was 84 wt % active material, 10 wt % conductive additive, 4 wt % sodium carboxymethyl cellulose binder, and 2 wt % styrene–butadiene rubber binder. Disks with a diameter of 0.5 in were punched out of the film. Typically, the mass of active material in the electrodes was between 1 and 1.5 mg cm^{-2}. The electrode disks were placed in 2032 coin cells in a half-cell configuration with metallic lithium as the counter electrode. A Celgard 3501 polypropylene membrane was used as the separator. A commercial electrolyte (1 M $LiPF_6$ in a 1/1/1 mixture by volume of ethylene carbonate, dimethyl carbonate, and diethyl carbonate) purchased from MTI Corp. was used in the cells. Coin cell assembly was performed in a glovebox filled with helium gas. Cells were tested using an Arbin Instruments BT-2000. Cycling was conducted between 1 and 3 V vs Li/Li^+. The C rate was set so that 1 C = 335 mA per gram of TiO_2 in the electrode.

Impedance spectroscopy was carried out on the coin cells by using a Solartron 1255B frequency response analyzer with an attached SI1287 electrochemical interface. The electrode film served as the active electrode, while lithium foil served as the reference and counter electrodes. A frequency range of 50 kHz to 50 mHz was used, along with an ac signal of 20 mV. During the measurement, a constant potential of 2.1 V vs Li^+/Li was applied. The impedance spectra were fitted to equivalent circuits using Wolfram Mathematica 9.

RESULTS AND DISCUSSION

Structural Characterization of TFA-TiO_2/C and acac-TiO_2/C. Numerous variables can be altered in the synthesis of the composite materials, but three variables are the main focus of this section: the type of chelating agent used in the synthesis, the pyrolysis temperature attained by the composite, and the use of carbon as a secondary template.

Two different chelating agents were used to stabilize the titanium isopropoxide in the multiconsitituent precursor. Without chelation, TiO_2 quickly precipitates out of the precursor prior to complete infiltration of the template. Trifluoroacetic acid had previously been used for arresting the condensation of a precursor that contained titanium alkoxide, allowing for the successful synthesis of mesoporous TiO_2 and 3DOM TiO_2.[44,45] 2,4-Pentanedione is another chelating agent commonly used to prevent rapid condensation of titanium alkoxides.[46] Both agents yielded precursors stable enough for the infiltration process. The overall TiO_2 content in the pyrolyzed composites was also similar: TFA-TiO_2/C pyrolyzed at 800 °C was 74 wt % TiO_2, while acac-TiO_2/C pyrolyzed at 800 °C was 71.5 wt % TiO_2. In addition to the TiO_2 content, elemental analysis was used to calculate fluorine content for the TFA-TiO_2/C pyrolyzed at 800 °C. Within the detection limits of the technique (0.25 wt %), no fluorine was found in the samples. While this does not completely eliminate possible low-level fluorine ion doping in the materials made via the TFA precursor, we postulate that fluorine does not play a significant role in the overall electrochemical properties.

Figure 1 shows PXRD patterns of both TFA- and acac-TiO_2/C composites together with the temperature reached during the final pyrolysis step. Carbon and four polymorphs of TiO_2 are observed in the patterns. While no strong peak exists for the amorphous carbon, a broad shoulder (essentially, a sloping background) is observed below 40° 2θ for all samples. Unlike the carbon, the TiO_2 present in both TFA-TiO_2/C and acac-TiO_2/C undergoes several phase transformations at different pyrolysis temperatures. At the lowest pyrolysis temperatures,

dx.doi.org/10.1021/ic402648f | Inorg. Chem. 2014, 53, 1100–1112

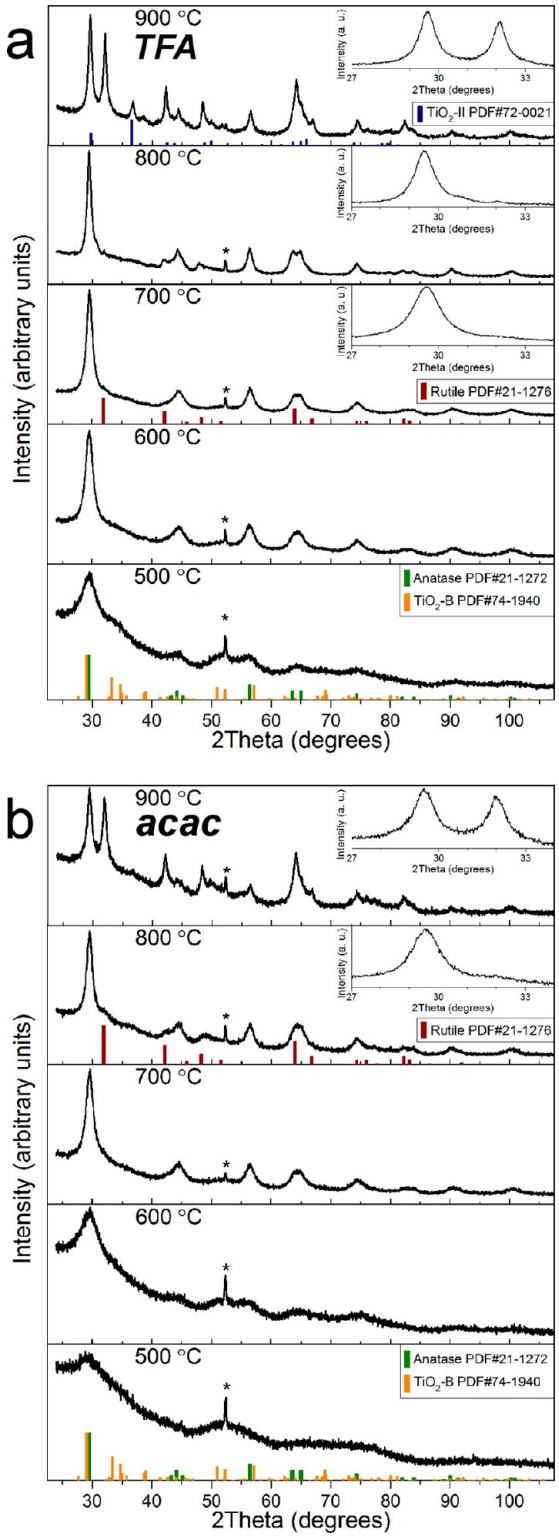

Figure 1. PXRD patterns of (a) TFA-TiO_2/C and (b) acac-TiO_2/C composites. The temperature reached in the final pyrolysis step is given. Reference patterns are presented underneath the collected patterns. The insets highlight the main reflections of anatase and rutile. The asterisk indicates a reflection from the Al sample holder.

anatase coexists with the monoclinic TiO_2-B phase. Identification of TiO_2-B is fairly uncomplicated due to the appearance of two overlapping peaks near 52°2θ (Figure 1). In syntheses with TiO_2 sol–gel precursors and surfactants, TiO_2-B can appear as a minor phase when the resulting materials are thermally treated at temperatures from 400 to 600 °C.[13,47,48] This is also observed with our composite materials. Even the relatively featureless pattern for acac-TiO_2/C pyrolyzed at 500 °C contains a very broad peak between 50 and 55° 2θ (Figure 1b). This feature is the result of several overlapping TiO_2-B reflections. It is important to note that the thermal stability of the TiO_2-B phase is quite high for these materials,[48] with acac-TiO_2/C retaining the phase at 600 °C. We ascribe this stability to the carbon matrix that impedes crystal growth and consequent transformation to the anatase phase.

As stated above, both TFA-TiO_2/C and acac-TiO_2/C contain the reflections characteristic of anatase TiO_2 (Figure 1). The main (101) reflection is clearly observed at ∼29.4° 2θ for all samples. Anatase is the majority phase detected in sol–gel syntheses when TiO_2 first crystallizes during thermal treatment, especially with syntheses conducted at low pH.[49,50] This can be ascribed to the fact that anatase is the thermodynamically stable polymorph for high-surface-area TiO_2 crystallites below ∼14 nm in size.[51,52] As the pyrolysis temperature increases, transformation from the anatase to the rutile polymorph accompanies an increase in crystallite size, since rutile is the thermodynamically stable phase for bulk TiO_2.[49] In TFA-TiO_2/C, the rutile (110) peak at ∼31.9° 2θ appears when the final pyrolysis temperature reaches 700 °C. Rutile remains a very minor phase until the pyrolysis temperature reaches 900 °C, when rutile becomes the majority phase. For acac-TiO_2/C, a similar sequence of phase transformation with respect to temperature is observed; however, the pyrolysis temperature has to reach 800 °C before rutile peaks appear. Both the acac- and TFA-TiO_2/C composite materials clearly stabilize the anatase phase at high temperatures, consistent with other reports on TiO_2/C composites.[37,39,53,54] A delay in the phase transformation is caused by the carbon matrix that confines the TiO_2 crystallites and prevents diffusion of ions/vacancies. Grain growth is therefore lessened and the crystallites do not grow to the diameter required for the transformation from anatase to rutile. Also, nucleation of the rutile phase at the interface of anatase crystallites is limited due to confinement.[55]

Estimates of crystallite size were made using the line broadening of the PXRD reflections (Table 1). TiO_2-B reflections were too weak to be adequately fit and were not analyzed. Unsurprisingly, crystallite size increases for the anatase grains as pyrolysis temperature increases. The crystallite growth is more pronounced for TFA-TiO_2/C samples. This can be observed starting with samples pyrolyzed at 500 °C. With acac-TiO_2/C, the reflections are so broad that it is not possible to accurately assess crystallite size. In contrast, TFA-TiO_2/C has an estimated grain size of 3.0 nm after pyrolysis at 500 °C. For acac-TiO_2/C, pyrolysis temperatures have to be increased by 100 °C to obtain an estimated crystallite size that corresponds to those in TFA-TiO_2/C (e.g., the crystallites in TFA-TiO_2/C at 700 °C are similar in size to acac-TiO_2/C at 600 °C). Larger crystallites negatively impact overall electrode performance, an important point that will be quite relevant in the subsequent discussion of these materials. By 900 °C, both samples contain anatase crystallites over 10 nm in size. Again, this is close to the predicted size range where rutile becomes the thermodynamically stable phase;[51] therefore, it is understandable that rutile is the major phase for samples pyrolyzed at 900 °C. Rutile also exhibits a larger crystallite size for both

dx.doi.org/10.1021/ic402648f | Inorg. Chem. 2014, 53, 1100–1112

Table 1. Structural and Textural Parameters of the 3DOM TiO_2/C Samples

sample	anatase crystallite size (nm)	rutile crystallite size (nm)	BET surface area (m^2/g)	pore volume (cm^3/g)	QSDFT micropore SA (m^2/g)[a]
TFA-TiO_2/C, 500 °C	3.0		261	0.24	172
TFA-TiO_2/C, 600 °C	5.8		332	0.46	222
TFA-TiO_2/C, 700 °C	8.5	*b*	394	0.44	244
TFA-TiO_2/C, 800 °C	11.5	*b*	451	0.46	232
TFA-TiO_2/C, 900 °C	14.0	15.8	505	0.63	304
acac-TiO_2/C, 500 °C	*c*		262	0.75	86.7
acac-TiO_2/C, 600 °C	3.0		272	0.56	144
acac-TiO_2/C, 700 °C	5.8		378	0.86	252
acac-TiO_2/C, 800 °C	8.4	*b*	428	0.50	277
acac-TiO_2/C, 900 °C	10.3	10.8	490	0.94	276
3DOM TiO_2	7.8		126	0.32	*d*

[a]Calculated using a QSDFT kernel for adsorption of N_2 on carbon at 77 K. [b]Rutile (110) peak too weak to accurately fit. [c]Anatase (101) line width too broad to accurately fit. Crystallite size is below 2 nm. [d]Sample devoid of carbon; therefore, QSDFT was not used.

types of composite; this is consistent with observations that rutile crystallites grow faster than anatase crystallites.[56]

One final note should be made about the PXRD patterns: a set of anomalous peaks are present in the TFA-TiO_2/C composite pyrolyzed at 900 °C. An intense peak is clearly observed near 36.5° 2θ, and others can be found in the pattern (Figure 1a). In the presence of carbon, TiO_2 can undergo carbothermic reduction to form various Magnelí phases with ordered defect structures.[53] Titanium carbide can also be formed.[57] None of the reduced phases of TiO_2 or TiC have a diffraction pattern that matches the additional peaks. Instead, the peaks match an orthorhombic phase of TiO_2 (TiO_2-II) that is generally synthesized by subjecting TiO_2 to high pressures.[58] We cannot fully explain the presence of TiO_2-II, but it may be related to the reduction of TiO_2. The high-temperature form of Ti_3O_5, β-Ti_3O_5, has an orthorhombic lattice (related to the pseudo-brookite structure).[59] It may be possible that a phase transition occurred from the Ti_3O_5 form to TiO_2-II when the sample was exposed to oxygen. Alternately, stresses induced by the confinement of TiO_2 in the 3DOM framework that contains carbon might induce the shear necessary for transformation to TiO_2-II.

More information concerning the crystal polymorphs present in the composite materials was obtained through confocal Raman microscopy. As is shown in Figure 2, characteristic vibrational modes for certain TiO_2 crystal structures can be found in TFA- and acac-TiO_2/C samples.[60] TiO_2-B modes, albeit extremely weak (Figure 2, orange arrows), are present in the spectra of composites that have TiO_2-B reflections in their XRD patterns. The anatase E_g mode centered near 150 cm^{-1} is generally the strongest mode in any given spectrum, a typical observation when examining nanocrystalline anatase that has long-range order.[61] Since the grain size for the anatase is below 20 nm in the samples, no sharp peaks were observed in the spectra of any of the samples. This can be explained by phonon confinement that results in broadening of Raman modes for small crystallites.[61]

At high pyrolysis temperatures, the anatase modes, most notably the E_g mode, lose intensity. Rutile vibrational modes, especially the E_g and A_{1g} modes, appear as the transformation from anatase to rutile begins. For TFA-TiO_2/C, rutile vibrational modes are found in various areas of the composite starting at 700 °C (Figure 2a). By 900 °C, the rutile modes dominate most spectra, and only weak peaks are observed that correspond to anatase modes. Some areas contain fairly intense anatase modes (top inset in Figure 2a), which might be indicative of regions with low TiO_2 content and consequently less sintering. Alternately, local variations in temperature during pyrolysis might contribute to the heterogeneity. Rutile peaks and heterogeneities in the observed polymorphs are also observed for acac-TiO_2/C composites. However, the pyrolysis temperature has to reach 800 °C before rutile modes are observed. The peak near 400 cm^{-1} shifts and a shoulder appears for some spectra due to the rutile E_g peak (see inset in Figure 2b). Even then, rutile remains a minor phase. Scanning a specific area, we determined that acac-TiO_2/C pyrolyzed at 900 °C contains rutile, and the modes are most intense on the surface of the monolithic pieces (see inset in Figure 2a). Any excess precursor left on the sample forms an untemplated surface "crust" after processing. Sintering can be quite severe in these regions, since large clusters of TiO_2 are aggregated on the surface. These observations all serve to largely confirm the data gathered from the XRD patterns. Furthermore, they indicate that the relative abundance of anatase vs rutile is not uniform for samples pyrolyzed at high temperatures.

In addition to providing information on the structure of TiO_2, Raman spectroscopy was conducted on the D/G bands for the carbon framework. These bands are related to specific vibrational modes in aromatic six-membered rings. The G band is found in pristine graphite (or planar sp^2 carbon) and comes from bond stretching. In contrast, the D band comes from a breathing mode that can only occur in carbon materials that contain disorder.[62] Figure S1 in the Supporting Information shows, for all of the samples, the region of the Raman spectra that contains the D/G bands. The same general trend is observed for both TFA-TiO_2/C and acac-TiO_2/C. As the pyrolysis temperature increases, the intensity of the D band increases relative to the G band (Table S1 in the Supporting Information). This may seem surprising at first glance, since the conductivity of hard, amorphous carbon derived from phenolic resins is known to increase with increasing temperature.[63,64] However, the intensity of the G peak has been reported to decrease with increasing pyrolysis temperature below 1000 °C for carbonized phenolic resins.[65] Ferrari and Robertson note that, for small (<2 nm) clusters of aromatic rings in amorphous carbon, the D band intensity increases as the cluster size becomes larger.[62] In our case, the observed increase in D band intensity is simply a reflection of the presence of more aromatic rings in the minute clusters that make up the amorphous carbon.

dx.doi.org/10.1021/ic402648f | Inorg. Chem. 2014, 53, 1100−1112

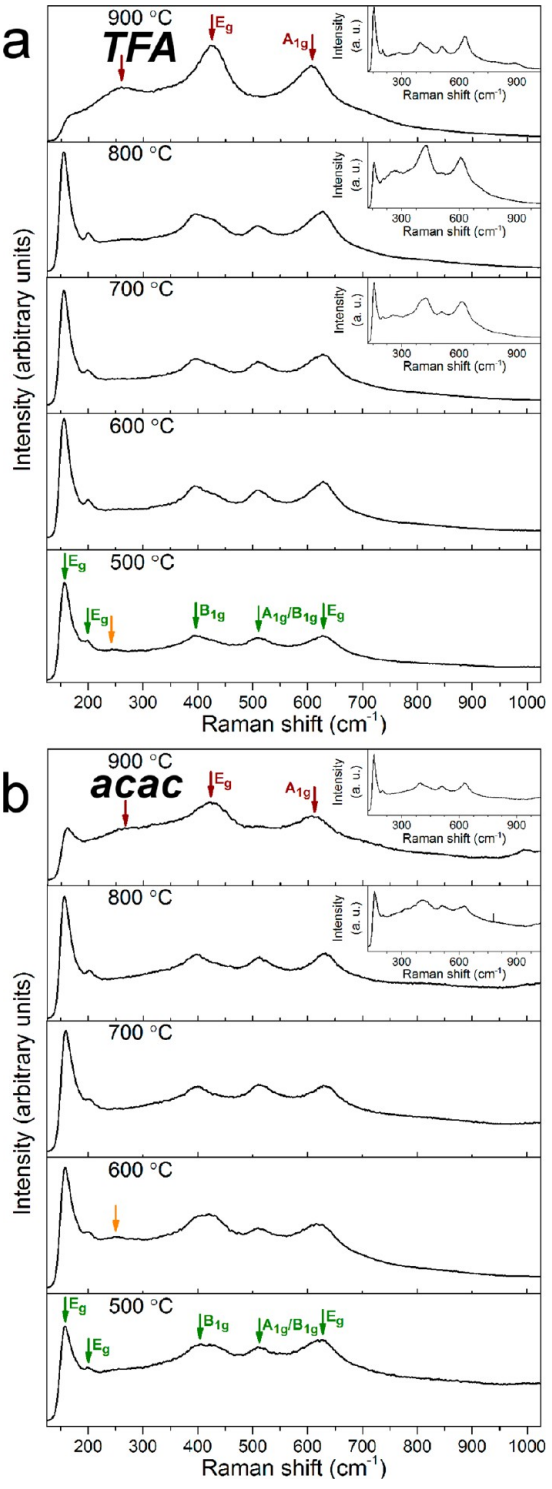

Figure 2. Raman spectra of (a) TFA-TiO_2/C and (b) acac-TiO_2/C. These spectra are from the region where TiO_2 lattice vibrations can be observed. Pyrolysis temperatures are given next to corresponding spectra. Arrows have been placed over some of the characteristic modes for anatase, rutile, and TiO_2-B in the spectra. The insets show the variation in the crystal polymorphs observed across a sample.

An assessment of the structure of the 3DOM network was conducted using SEM. Figure 3 contains a panel of SEM images for all TFA- and acac-TiO_2/C pyrolyzed at different temperatures. In all of the images, the face-centered cubic (fcc) lattice of macropores is clearly visible. Interconnecting windows are present between the large macropores, but unlike the case for the larger macropores, there is variation in the diameter of the windows.

Differences in crystallite size and location can also be ascertained using SEM for some of the composites. Figure S2 in the Supporting Information highlights the significant difference in crystallite size between TFA- and acac-TiO_2/C in the materials pyrolyzed at 800 °C. The aggregation is more pronounced in TFA-TiO_2/C, as is expected from the PXRD patterns. This trend continues at higher temperatures as well. SEM micrographs also suggest that a substantial fraction of the TiO_2 exists on the surface of TFA-TiO_2/C samples.

More information concerning the textural properties of the composites can be determined using N_2 sorption. This includes information concerning the presence of any mesopores created by the surfactant present in the precursor. The sorption isotherms for TFA- and acac-TiO_2/C are presented in Figure S3 in the Supporting Information. An analysis of the general shape of the isotherms yields several insights into the porosity present in the composites. First, the hysteresis that is characteristic of mesoporous materials is absent for the majority of the isotherms. Weak hysteresis is observed for the samples pyrolyzed at 500−600 °C and also at 900 °C. The hysteresis at 900 °C is clearly not related to the surfactant template. Second, a sharp rise in the isotherm at $P/P_0 > 0.9$ reflects the presence of macroporosity. Third, another sharp rise is present at very low P/P_0 that comes from microporosity in the amorphous carbon matrix.[66] Finally, closure of the isotherms does not occur for the samples pyrolyzed at 500 °C. Many polymeric materials (such as the PF resin) have isotherms that do not close,[66] which would explain why this phenomenon happens only at low temperatures.

Table 1 presents additional information derived from the isotherms. Examining the BET surface areas first, an increase in surface area is observed as the pyrolysis temperature increases. This is in line with reports on mesoporous TiO_2/C composites derived using PF sol.[37,53] Much of this increase can be attributed to the development of microporosity in the carbon phase. An estimate of the micropore area was found via a quenched state density functional theory (QSDFT) kernel for carbon. While the fits to the isotherms are good, we can only consider this an estimate due to differences in surface energetics between carbon and TiO_2. In general, the surface area due to microporosity increases for both TFA- and acac-TiO_2/C at higher pyrolysis temperatures, which can be attributed to the carbon in the composites. It is likely that the majority of the BET surface area increase is from the carbon, but mesoporosity that arises from the spaces between TiO_2 grains may also contribute. Since micropores in the carbon will not greatly increase the capacity of the composite material in the 1−3 V range,[54] the enhanced surface areas are not a major factor in the electrochemical performance of these composites. Pore volume does not follow a clear trend with increasing pyrolysis temperature for either TFA- or acac-TiO_2/C. At high P/P_0, there is a sharp increase in the volume adsorbed. Some factor other than the geometry of the 3DOM network may be responsible, including breakdown of the material into smaller particles.

Since only limited evidence of mesoporosity was found with gas sorption, we used SAXS to obtain evidence that a mesostructure exists in some of the composites. Before pyrolysis, the infiltrated, thermally treated TFA- and acac-TiO_2/C both have a broad peak in their SAXS patterns (Figure

dx.doi.org/10.1021/ic402648f | Inorg. Chem. 2014, 53, 1100−1112

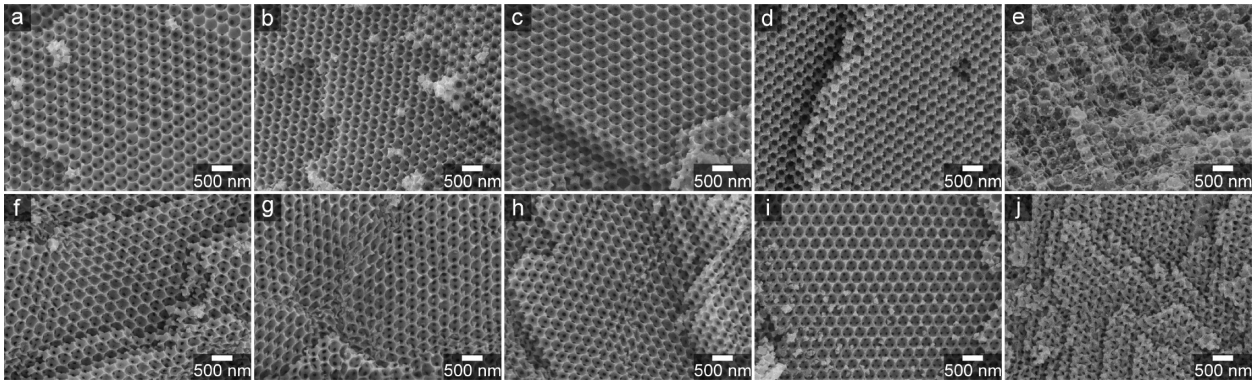

Figure 3. SEM images of TFA-TiO_2/C (a–e, 500–900 °C, 100 °C increments) and acac-TiO_2 composites (f–j, 500–900 °C, 100 °C increments). The 3DOM morphology is present in all of the materials processed. A well-ordered 3DOM morphology is observed across the majority (>50%) of any given sample.

S4 in the Supporting Information). The peak in the patterns comes from a disordered mesostructure that arises from the coassembly of surfactant molecules with other components of the precursor. Differences in *d* spacing are observed between peaks in the patterns for TFA- and acac-TiO_2/C (10.0 nm versus 12.3 nm). Even though the same block-*co*-polymer was used as the soft template for both syntheses, the type of chelating agent and amounts of solvent used were changed. This change could result in a difference in the swelling of any P123 micelles and explain the altered *d* spacing.[41] Once the samples are pyrolyzed, the disordered mesopore network disappears (Figure S5 in the Supporting Information). Weak scattering peaks are observed for TFA-TiO_2/C at 6.9 nm (the contraction is due to condensation and shrinkage of the 3DOM network) until pyrolysis at 600 °C. The acac-TiO_2/C material fares better with regards to mesostructural stability; a weak scattering peak at 8.9 nm does not disappear until pyrolysis at 800 °C. Mesostructural collapse in both types of composite is likely a result of the sintering of TiO_2 crystallites. If pores are present in the TiO_2 phase, thermally induced densification will ultimately close them. Pores present in the carbon phase can undergo collapse as growing TiO_2 crystallites pierce through their sides. Since acac-TiO_2/C has a consistently smaller crystallite size than TFA-TiO_2/C, better mesostructural stability is expected.

TEM analysis of the TiO_2/C composites further confirms these experimental results. TiO_2 crystallites contained within the walls of the 3DOM structure gradually increase in size as the pyrolysis temperature increases, due to thermally induced grain growth. Figure 4 shows this effect and also demonstrates the impact of chelating agent; crystallites present in acac-TiO_2/C are considerably smaller than crystallites in TFA-TiO_2/C. Additionally, as the pyrolysis temperature exceeds ~700 °C for TFA-TiO_2/C, the crystallites become larger than the confines of the walls. With increasing temperature, the TiO_2 grows outward, no longer contained by the carbon framework (Figure S6 in the Supporting Information). This may result in poorer performance due to loss of carbon/TiO_2 interfacial area. Finally, low pyrolysis temperatures are associated with retention of disordered mesoporosity within the walls of the structure, offering confirmation of the SAXS results (Figure S7 in the Supporting Information).

From the structural analysis conducted above, there are clear differences caused by the use of trifluoroacetic acid vs 2,4-pentanedione as a chelating agent. No matter what chelating

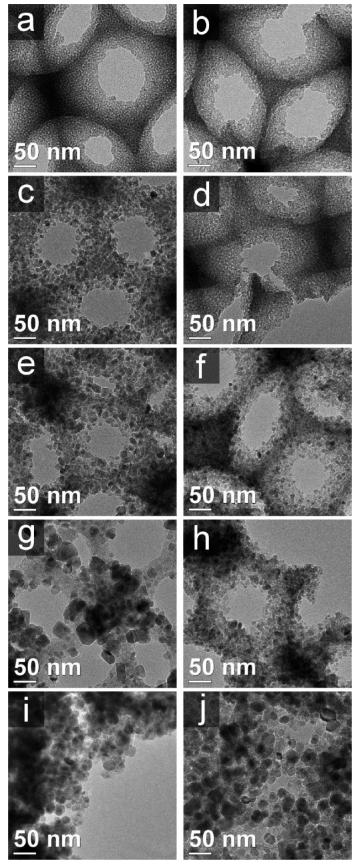

Figure 4. TEM images of TFA-TiO_2/C (a, c, e, g, and i, 500–900 °C, 100 °C increments) and acac-TiO_2/C (b, d, f, h, and j, 500–900 °C, 100 °C increments) composites. The TiO_2 crystallite size increases as the pyrolysis temperature is increased. At higher temperatures, the substantially larger TiO_2 crystallites present in TFA-TiO_2/C are clearly observed in comparison to images from acac-TiO_2/C.

agent is used, TiO_2 crystallites can be found embedded in the carbon phase. However, TEM and SEM imaging reveals that the TiO_2 crystallites in TFA-TiO_2/C are concentrated on the exterior surface of the 3DOM network. This localization also results in enhanced sintering and crystal growth of TiO_2, despite the fact that TFA-TiO_2/C has a carbon content nearly identical with that of acac-TiO_2/C. The origin of the pronounced differences in the distribution of TiO_2 lies in the compatibility of the chelated complex with the other

dx.doi.org/10.1021/ic402648f | *Inorg. Chem.* 2014, 53, 1100–1112

components of the precursor. When trifluoroacetic acid is used to chelate titanium isopropoxide (in a 1/1 molar ratio), the resulting complex contains numerous trifluoromethyl groups.[44] Most of the other components of the precursor (water, alcohols, and the resol clusters) contain O−H moieties that can participate in hydrogen bonding. Interactions between the hydrophobic titanium-containing complex and the rest of the precursor should be unfavorable for TFA-TiO_2/C. Separation of the complex to the relatively hydrophobic surface of the PMMA template should then occur, in line with what we observe. A far different result should be expected for the acac-TiO_2/C precursor. Prior studies in the literature have determined that various monomers and dimers form when 2,4-pentanedione and titanium alkoxides are combined in solution.[46,67] No matter what particular complexes are found in the precursor, these titanium-containing complexes will contain aquo and hydroxo groups that can participate in hydrogen bonding. Since the complexes in the acac-TiO_2/C precursor are relatively hydrophilic, they should be well distributed throughout the other components of the precursor. Ultimately, this would lead to a situation where TiO_2 condenses and nucleates throughout the interstitial space of the colloidal crystal template. The surrounding carbon can more effectively restrict the growth of TiO_2 crystals and impede sintering, explaining the reduced crystal size for acac-TiO_2/C.

TFA-TiO_2/C and acac-TiO_2/C exemplify two possible distributions of an active material in a secondary matrix for a 3DOM/m nanocomposite. Taking these materials and a 3DOM/m $LiFePO_4$/C composite described by Vu and Stein into consideration,[68] three distinct types of 3DOM/m metal oxide/phosphate and carbon composites can be identified. Figure 5 offers computer renderings highlighting the difference in the distribution of the active phase in the three composites. In Figure 5a, the active material is confined in confined in the octahedral nodes, as in the case for the 3DOM/m $LiFePO_4$/C. The precursors for $LiFePO_4$ are more ionic and minimize interactions with the nonpolar PMMA template by aggregating in the octahedral nodes.[68] Figure 5b shows an intermediate distribution where the active material is distributed throughout the composite. This is observed for acac-TiO_2/C, owing to the favorable interaction between the titanium complex and the other components of the precursor. Finally, Figure 5c is the other extreme case, where the active material is primarily localized on the outer surface. Unfavorable interactions between the titanium complex and the other precursor components lead to the situation shown in Figure 5c for TFA-TiO_2/C. It is clear that the structure of the metal complex can dictate overall positioning of the active material in the carbon composite. Future work on templated composites should consider optimization of the interactions between any metal-containing complex, the solvent, additional precursors, and a hard template to achieve a distribution of active material favorable for the application at hand.

Structural Characterization of 3DOM TiO_2. Before moving on to a discussion of the anodes made from the composites, one other material needs to be discussed: the 3DOM TiO_2 produced using carbon as a secondary template. This material was obtained by calcination of TFA-TiO_2/C pyrolyzed at 500 °C. The choice of TFA-TiO_2/C was made due to its slightly higher TiO_2 content in comparison to that of acac-TiO_2/C. In this initial step, the crystallite size was minimized both by the low pyrolysis temperature and the presence of a confining partially carbonized phase. Burnout of

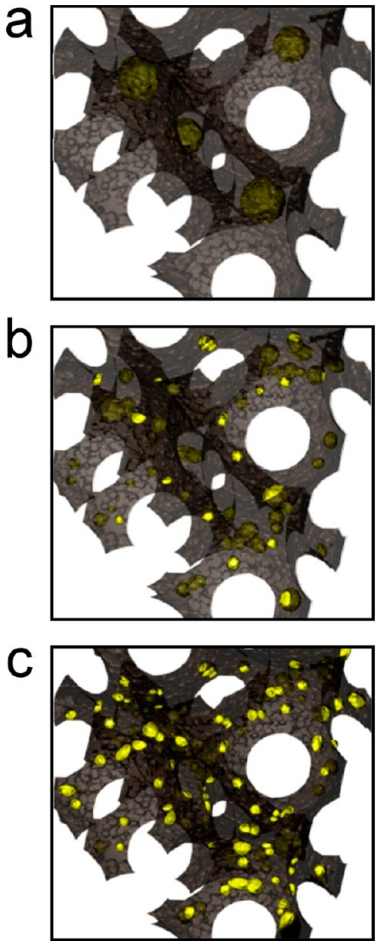

Figure 5. Computer renderings of three different distributions of an active material (yellow) in a secondary matrix (brown) for 3DOM/m composites. In (a) the active material is localized in the octahedral nodes, in (b) the active material is well-distributed through the structure, and in (c) the active material is localized on the exterior surface.

the partially carbonized PF resin increased the crystallite size of the anatase phase, as shown by the clear decrease in the line width of the XRD peaks (Figure 6a and Table 1). Also, the shoulder below 40° 2θ from the PF component disappeared. The material retained a BET specific surface area of 126 m^2/g (Figure 6b and Table 1), which is a value similar to that obtained in mesoporous TiO_2 made using soft templating.[10] SEM micrographs reveal that the 3DOM structure is preserved after the combustion of the carbon matrix (Figure 6c). Some variation in the size of interconnecting windows is present in the 3DOM structure and likely arose from the original composite (Figure S9 in the Supporting Information). Finally, TEM imaging (Figure 6d) reveals that the walls and nodes of the 3DOM network are comprised of aggregated TiO_2 crystallites. Textural mesoporosity exists between the crystals (enhanced by removal of the carbon phase), but no ordered mesoporosity can be found.

Electrochemical Characterization. The TFA-TiO_2/C and acac-TiO_2/C composites pyrolyzed at 800 °C and the 3DOM TiO_2 were selected for electrochemical tests and processed into electrodes for the half-cells. The choice for the pyrolysis temperature was made by taking two factors into consideration. First, the PF resin needs to be brought to a sufficiently high temperature to adequately carbonize that

dx.doi.org/10.1021/ic402648f | Inorg. Chem. 2014, 53, 1100−1112

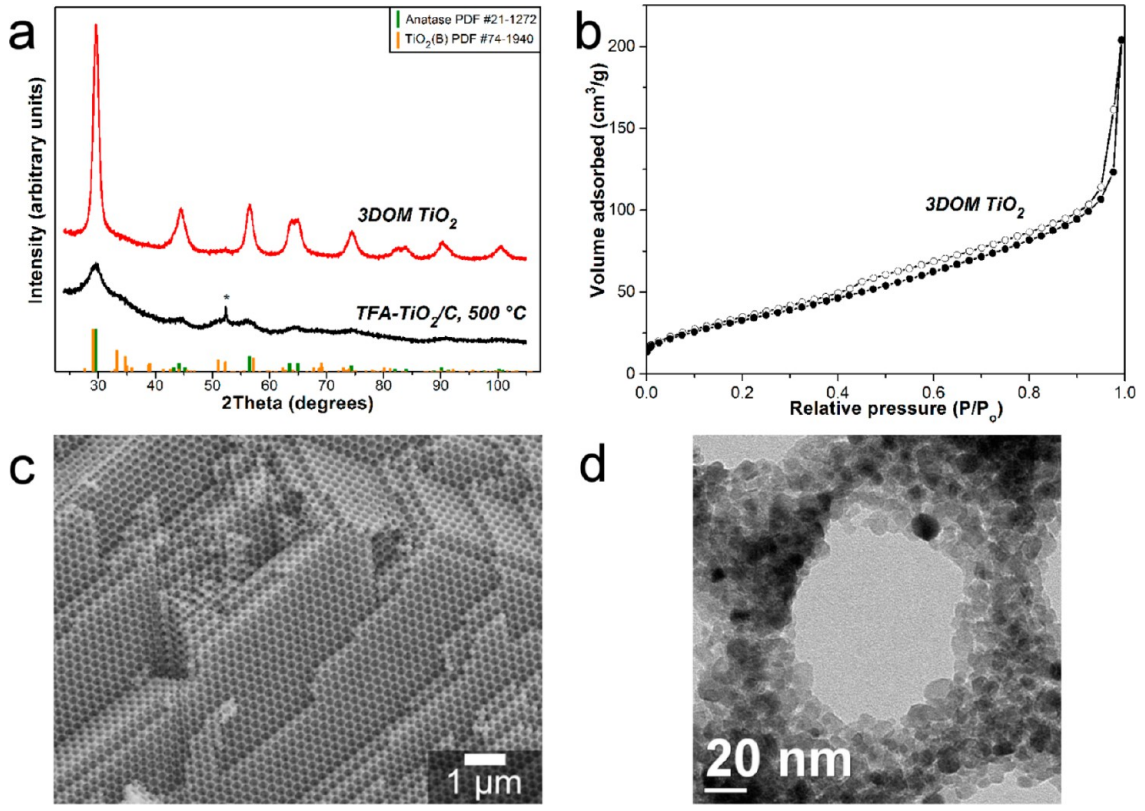

Figure 6. Characterization of the 3DOM TiO_2 produced from TFA-TiO_2/C pyrolyzed at 500 °C: (a) PXRD patterns of the original composite and 3DOM TiO_2; (b) nitrogen sorption isotherm for the 3DOM TiO_2; (c) SEM and (d) TEM images showing the 3DOM network that is made from fused TiO_2 crystallites.

particular component of the composite. As observed in Figure S1 (Supporting Information), the Raman D band intensity increases at higher temperatures for the composites, indicating that the degree of graphitization increases. It is also known from dc conductivity testing using carbonized phenolic resin and carbonized 3DOM resorcinol–formaldehyde that temperatures in excess of 700 °C are needed to obtain conductivities near 10 S m^{-1}.[63,64] However, the crystallite size increases substantially as the pyrolysis temperature increases (Table 1). As a compromise, 800 °C was chosen for a comparison between the capacity of TFA-TiO_2/C and acac-TiO_2/C at different rates.

Figure 7a shows the results of electrochemical lithiation and delithiation cycles at different rates for the composites pyrolyzed at 800 °C and 3DOM TiO_2. At all rates, the capacity of acac-TiO_2/C is significantly higher than that of TFA-TiO_2/C. Clearly, the decreased TiO_2 crystallite size in acac-TiO_2/C can account for most of the capacity boost. Aside from crystal size, another contributing factor could be the location of the TiO_2 crystallites in the matrix. In TFA-TiO_2/C, crystallites are observed in sizable clusters on the surface. Electronic and ionic transport through the TiO_2 aggregates is then constrained to the contact points with the carbon matrix.[31] In contrast, acac-TiO_2/C contains many TiO_2 crystallites embedded in the carbon matrix, which might lead to better "wiring" for the TiO_2. The voltage profiles of the materials cycled in Figure 7a are shown in Figure S8 in the Supporting Information. A characteristic plateau is observed in the profiles that results from the coexistence of a lithium-poor tetragonal and lithium-rich orthorhombic phase.[29] For the two composites, a greater contribution comes from a voltage range below the plateau region. This could be from small crystallites that can undergo primarily solid solution storage[22] or from intercalation into the carbon phase itself.

Perhaps the most surprising result in Figure 7a is the excellent capacity of the 3DOM TiO_2 relative to the composites. At high rates, the capacity of 3DOM TiO_2 is greater than that of both composites. When the total mass of the electrode is taken into account (active and inactive components), 3DOM TiO_2 has the highest capacity, even at slow charge/discharge rates. The capacity boost in this compositionally simpler material may originate from several factors. First, crystallite size in the 3DOM TiO_2 is smaller (7.8 nm) than the TiO_2 crystallites in the composites (11.4 nm for TFA-TiO_2/C and 8.5 nm for acac-TiO_2/C) due to the lower temperatures needed for processing. Second, burnout of the secondary carbon template produces numerous void spaces. These pores allow for penetration of the electrolyte throughout the structure, shortening diffusion lengths. With acac-TiO_2/C, numerous TiO_2 particles are buried in the carbon network, which restricts lithium ion transport. Finally, the only conductive additive in the 3DOM TiO_2 electrode is Super P carbon black. This carbon black has an electronic conductivity higher than the amorphous carbon present in the composites. Electronic transport through the amorphous carbon network may be a hindrance during rapid charging/discharging.

To further investigate the effects of the pyrolysis temperature, acac-TiO_2/C materials pyrolyzed at 700, 800, and 900 °C were processed into electrodes and tested. The results are shown in Figure 7b. These pyrolysis temperatures are within the range in which carbon should be suitably conductive for cycling.[64] Pyrolysis at 800 °C results in the highest capacities at

dx.doi.org/10.1021/ic402648f | Inorg. Chem. 2014, 53, 1100–1112

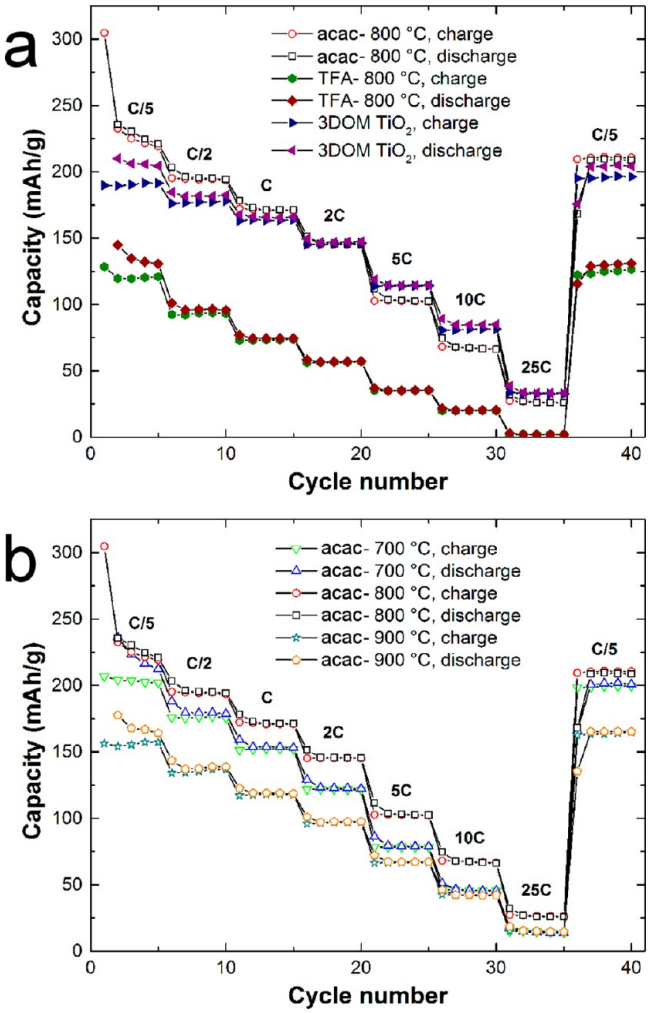

Figure 7. (a) Rate performance data for various samples, including TFA-TiO_2/C pyrolyzed at 800 °C, acac-TiO_2/C pyrolyzed at 800 °C, and 3DOM TiO_2. (b) Rate performance data for the acac-TiO_2/C pyrolyzed at 700, 800, and 900 °C. All specific capacities are plotted with respect to the mass of TiO_2 in the electrode.

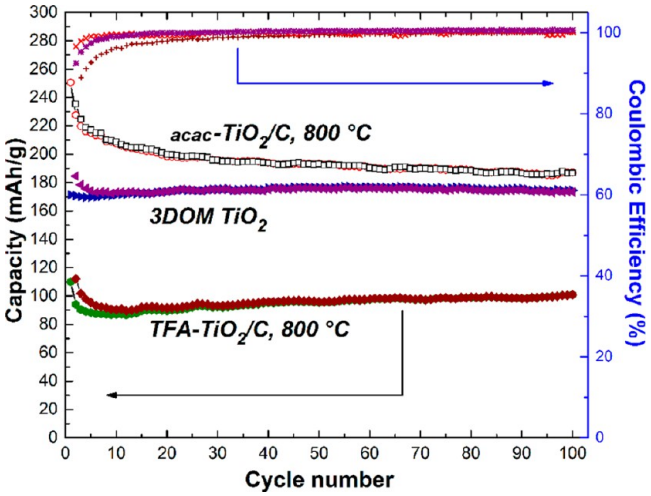

Figure 8. Cycle performance of TFA-TiO_2/C pyrolyzed at 800 °C, acac-TiO_2/C pyrolyzed at 800 °C, and 3DOM TiO_2 shown over 100 cycles. Coulombic efficiencies are also plotted for the materials (brown + from TFA-TiO_2/C, purple * from 3DOM TiO_2, and red × from acac-TiO_2/C). The rate was set at C/2.

all rates, validating the choice of pyrolysis temperature made earlier. However, acac-TiO_2/C pyrolyzed at 700 °C exhibits similar capacities, especially upon the return to cycling at a rate of C/5. Overall, Figure 7b demonstrates a major tradeoff that must be considered when using these composites as anode materials. While it is necessary to carbonize the PF resin at high temperatures, thereby increasing its conductivity, this necessity comes with a price. Crystallite size increases to the point at which diffusion through the large grains offsets any gains in carbon conductivity (i.e., acac-TiO_2/C at 900 °C).

The capacities of TFA-TiO_2/C, acac-TiO_2/C, and 3DOM TiO_2 after extended cycling at C/2 are shown in Figure 8. Coulombic efficiencies are good for the materials and exceed 99% after ca. 20 cycles. The order of charge/discharge capacities for the materials is the same as that observed in Figure 7a. The acac-TiO_2/C material has the highest capacities over all cycles, followed closely by 3DOM TiO_2, and TFA-TiO_2/C has the lowest capacity by a considerable margin. While acac-TiO_2/C has the best capacity, it suffers from a decay in capacity of roughly 25% when cycle 2 is compared to cycle 100. This decay in capacity has been observed in TiO_2/C composite systems;[69] thus, it is possible that the volume expansion and contraction during lithiation of TiO_2 (albeit small)[20] is damaging the contact between the carbon framework and the TiO_2. In contrast, the capacity of the 3DOM TiO_2 is fairly constant and the capacity of TFA-TiO_2/C increases. Any increases in capacity may be related to a more complete diffusion of electrolyte through a prepared electrode.[69]

Taking all of the cycling results into consideration, the materials attain capacities equal to or greater than that of the mass-produced, fumed TiO_2 Aeroxide P25. Capacities for the nanocrystalline P25 are comparable to those for TFA-TiO_2/C (Figure S9 in the Supporting Information); however, the carbon phase present in the composite appears to improve its performance at high rates. Both acac-TiO_2/C and 3DOM TiO_2 have significantly elevated capacities in comparison to P25 owing to reduced crystal sizes and interconnected pore walls.

The two materials with the highest capacities, 3DOM TiO_2 and acac-TiO_2/C pyrolyzed at 800 °C, possess lithium ion intercalation behavior that matches similar materials. With regard to the composite, for instance, equivalent capacities were reported for mesoporous, hollow TiO_2 spheres coated with amorphous carbon.[40] At a C/2 rate, some of these spheres composites have capacities of ~200 mAh/g, similar to that of acac-TiO_2/C (198 mAh/g). Additionally, acac-TiO_2/C compares favorably to ordered mesoporous TiO_2/C, when cycled at a rate of 2C (both have capacities of ~150 mAh/g).[54] It should also be noted that a larger voltage window was used for the mesoporous TiO_2/C (0–3 V vs Li^+/Li). The 3DOM TiO_2 also has capacities that exceed those of many other nanostructured TiO_2 materials. For instance, Jiang et al. synthesized 3DOM TiO_2 without a secondary template and achieved a capacity of 125 mAh/g at ~2 C.[70] Even with a lower weight percent of carbon black in the electrode (10 wt % versus 15 wt %), the 3DOM TiO_2 prepared in this report has a capacity of 145 mAh/g. However, when more conductive carbon materials are used, such as graphene and carbon fibers, greater capacities are attainable at high rates (i.e., <100 mAh/g at 30 C).[71,72] 3DOM TiO_2 also has capacities that match those of several different mesoporous TiO_2 materials at a rate of 1 C. Both mesoporous anatase[69,73] and rutile[74] have been produced that have

dx.doi.org/10.1021/ic402648f | Inorg. Chem. 2014, 53, 1100–1112

capacities slightly lower than the ~160 mAh/g achieved by 3DOM TiO_2. When TiO_2 crystallite size is decreased further than what is observed in 3DOM TiO_2 or porous TiO_2-B produced in a synthesis, it is possible to achieve even higher rates.[22,75,76] Still, it appears that the small crystallites and disordered pores that are present in the 3DOM TiO_2 structure are sufficient to allow for shortened diffusion lengths. This structure provides good performance at moderate cycling rates.

To further study the effect of the pyrolysis temperature and chelating agent on the electrochemical properties and kinetic processes of the electrode reaction, electrochemical impedance spectroscopy (EIS) was used, both before and after 10 cycles at C/2. The impedance spectra (Figure 9) show a depressed semicircle in the high- to medium-frequency regions and a linear section in the low-frequency region, as would be expected for a lithium insertion/deinsertion mechanism.[77] The spectra were fitted to the equivalent circuit shown in Figure 9c (see Table S2 in the Supporting Information for the calculated parameters). This circuit is comprised of a series resistor and capacitor (R_s and C_s, respectively), two elements each comprised of a parallel capacitor and resistor (R_1, R_2, C_1, and C_2), and a modified Randles cell (comprised of R_3, C_3, and Warburg impedance): a model similar to that for other TiO_2-based anodes.[77,78] Moving across the circuit, the series resistor models the electrical resistance of the cell casing, testing apparatus, electrodes, and electrolyte, while the series capacitor models reversible ion sorption on exposed, nonelectrode surfaces inside the cell. A series capacitor is not needed in all cases, specifically TFA-TiO_2/C and acac-TiO_2/C samples pyrolyzed at 800 °C. Both of the next capacitor/resistor elements model surfaces at the electrode within the cell. R_1 and C_1 model the SEI layer, electrode roughness, and ion transport across the surface, while R_2 and C_2 model surfaces that are relatively inaccessible to the electrolyte and have a high resistance (i.e., TiO_2 embedded in the carbon matrix, TiO_2 that suffers from poor electrolyte wetting).[77,79] In all samples except for the acac-TiO_2/C pyrolyzed at 700 °C, all of the resistances dropped, consistent with improved electrolyte wetting allowing for improved ionic conductivity. The anomaly may be a result of an SEI layer blocking access to the small, embedded crystallites of TiO_2. Overall, the sample with the best performance, acac-TiO_2/C pyrolyzed at 800 °C, has the lowest resistances.

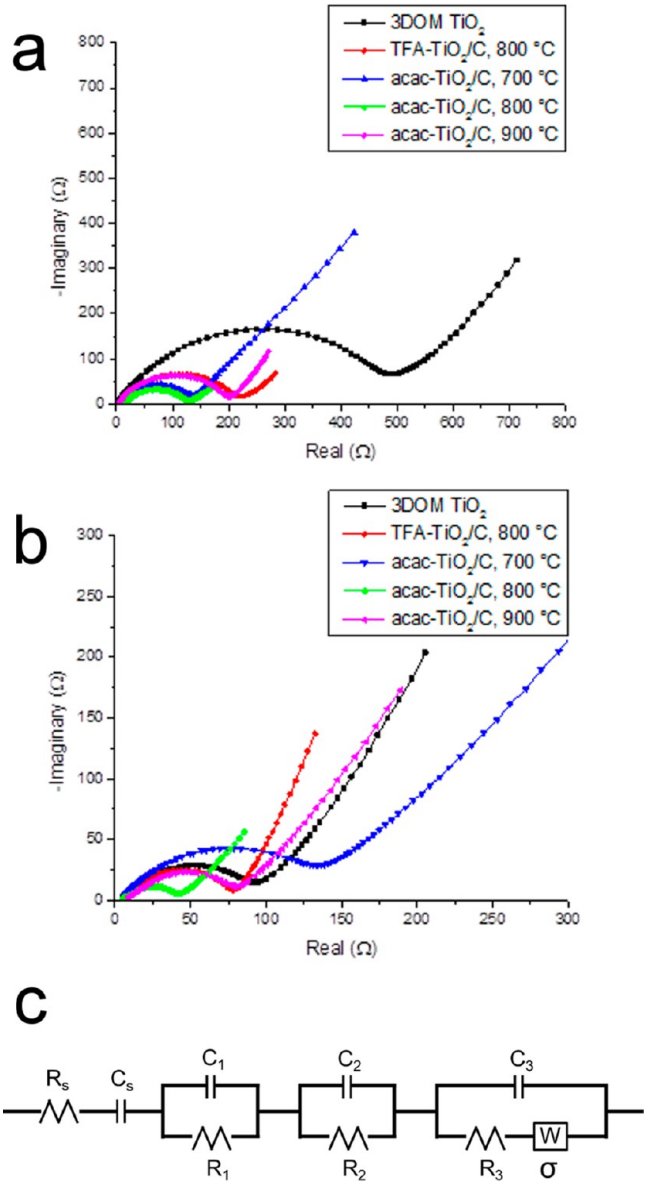

Figure 9. Nyquist plots of (a) as made coin cells and (b) cells after 10 cycles at C/2. The equivalent circuit used to model the impedance spectra is shown in (c).

Looking beyond the resistances, we see that the Warburg coefficient (σ) decreases after electrochemical cycling of the samples made with TFA, indicating an increase in the Li^+ diffusion coefficient.[80] In contrast, the samples made with acac show an increase in σ, indicating a decrease in the Li^+ diffusion coefficient. This is consistent with the overall trends observed in Figure 9, where TFA-TiO_2/C and 3DOM TiO_2 show an increase in capacity after repeated cycling, while the capacity in the acac-TiO_2/C decays. Interestingly, the values for σ in TFA-TiO_2/C compare favorably to those for acac-TiO_2/C, despite its poor performance during cycling. The lower than expected values for σ in TFA-TiO_2/C can be ascribed to the higher accessible TiO_2 surface area for this sample, since the grains are, in general, on the surface of the 3DOM network. However, while the Li^+ diffusion rate may be higher, the larger TiO_2 crystals found in that sample would limit the extent of discharge, leading to the overall lower capacity. This also explains why σ is lower for the acac-TiO_2/C pyrolyzed at 900 °C (a sample that has many crystallites protruding out of the carbon), in comparison to the sample pyrolyzed at 700 °C.

CONCLUSIONS

Through the analysis of two types of 3DOM/m TiO_2/C materials, we were able to investigate several variables that control the structure of these porous composites. By influencing the structural features, we optimized the lithium ion insertion properties for the anodes made from the TiO_2/C. The chelating agent used to stabilize the titanium alkoxide in the precursor has a great impact on the resulting structure of the composite. The relatively hydrophobic trifluoroacetic acid causes the formation of a titanium complex that segregates to the surface of the PMMA colloidal crystal template. As a consequence, when the pyrolysis temperature is altered, TFA-TiO_2/C experiences severe TiO_2 crystallite growth from the clustering of TiO_2 on the surface of the 3DOM network. In contrast, the hydrophilic complexes produced using 2,4-pentanedione as a chelating agent allow for distribution of

dx.doi.org/10.1021/ic402648f | Inorg. Chem. 2014, 53, 1100−1112

TiO_2 throughout the structure. These crystallites remain within the carbon phase, restricting overall crystallite growth. Ultimately, this results in a much higher capacity for reversible Li^+ intercalation than in the case of TFA-TiO_2/C. After pyrolysis at 800 °C, the acac-TiO_2/C displays excellent capacities (over 180 mAh/g at C/2), low resistances in the cell, and low Warberg impedance. However, burial of the TiO_2 grains in the carbon network may impede performance in certain cases. Removing the partially carbonized phase for TFA-TiO_2/C pyrolyzed at 500 °C results in the formation of 3DOM TiO_2 with additional porosity between TiO_2 crystallites. Since this material has an open structure with a fairly small crystallite size (<8 nm) that reduces overall diffusion lengths, its capacity (<160 mAh/g) at moderate lithiation and delithiation rates is comparable to that of the acac-TiO_2/C pyrolyzed at 800 °C. It can be envisioned that similar approaches to adjusting the chelating agent, pyrolysis temperature, and the presence of the carbon phase will allow for better structural control over other 3DOM/m composites. Improved performance for these materials in a wide range of applications (not just battery electrodes) could then be attained.

■ ASSOCIATED CONTENT

Supporting Information

Figures and tables giving additional Raman data, SEM/TEM images, nitrogen sorption isotherms, voltage profiles, rate performance data, and SAXS patterns. This material is available free of charge via the Internet at http://pubs.acs.org.

■ AUTHOR INFORMATION

Corresponding Author

*A.S.: tel, +1-612-624-1802; fax, +1-612-626-7541; e-mail, a-stein@umn.edu.

Notes

The authors declare no competing financial interest.

■ ACKNOWLEDGMENTS

This material is based upon work that was supported by the Department of Energy Office of Science under Award Number DE-SC0008662. N.D.P. and S.G.R. thank the University of Minnesota for Doctoral Dissertation Fellowships. A.M. thanks the S. N. Bose Scholars Program for a scholarship. The authors also thank Prof. Philippe Buhlmann for his assistance in the interpretation of impedance spectra, and Daniel Boman for his assistance with optimization of the TFA-TiO_2/C system, Professor William H. Smyrl for access to his dry room and electrochemical equipment, and Professor R. Lee Penn for use of her X-ray diffractometer. Parts of this work were carried out in the University of Minnesota Characterization Facility, which receives partial support from the NSF through the MRSEC, ERC, MRI, and NNIN programs.

■ REFERENCES

(1) Tachikawa, T.; Fujitsuka, M.; Majima, T. *J. Phys. Chem. C* **2007**, *111*, 5259−5275.
(2) Chen, X.; Shen, S.; Guo, L.; Mao, S. S. *Chem. Rev.* **2010**, *110*, 6503−6570.
(3) Kadoshima, M.; Hiratani, M.; Shimamoto, Y.; Torii, K.; Miki, H.; Kimura, S.; Nabatame, T. *Thin Soild Films* **2003**, *424*, 224−228.
(4) Lee, M.-J.; Seo, S.; Kim, D.-C.; Ahn, S.-E.; Seo, D. H.; Yoo, I.-K.; Baek, I.-G.; Kim, D.-S.; Byun, I.-S.; Kim, S.-H.; Hwang, I.-R.; Kim, J.-S.; Jeon, S.-H.; Park, B. H. *Adv. Mater.* **2007**, *19*, 73−76.
(5) Hagfeldt, A.; Boschloo, G.; Sun, L.; Kloo, L.; Pettersson, H. *Chem. Rev.* **2010**, *110*, 6595−6663.
(6) Jung, H. S.; Lee, J.-K. *J. Phys. Chem. Lett.* **2013**, *4*, 1682−1693.
(7) Auer, G.; Griebler, W.-D.; Jahn, B. White Pigments. In *Industrial Inorganic Pigments*, 3rd ed.; Buxbaum, G., Pfaff, G., Eds.; Wiley-VCH: Weinheim, Germany, 2005; pp 51−97.
(8) Comotti, M.; Li, W.-C.; Spliethoff, B.; Schüth, F. *J. Am. Chem. Soc.* **2006**, *128*, 917−924.
(9) Cao, A.; Lu, R.; Veser, G. *Phys. Chem. Chem. Phys.* **2010**, *12*, 13499−13510.
(10) Fröschl, T.; Hörmann, U.; Kubiak, P.; Kučerová, G.; Pfanzelt, M.; Weiss, C. K.; Behm, R. J.; Hüsing, N.; Kaiser, U.; Landfester, K.; Wohlfahrt-Mehrens, M. *Chem. Soc. Rev.* **2012**, *41*, 5313−5360.
(11) Huang, S. Y.; Kavan, L.; Exnar, I.; Grätzel, M. *J. Electrochem. Soc.* **1995**, *142*, L142−L144.
(12) Kavan, L.; Rathouský, J.; Grätzel, M.; Shklover, V.; Zukal, A. *J. Phys. Chem. B* **2000**, *104*, 12012−12020.
(13) Kavan, L.; Rathouský, J.; Grätzel, M.; Shklover, V.; Zukal, A. *Microporous Mesoporous Mater.* **2001**, *44*−*45*, 653−659.
(14) Leroux, F.; Dewar, P. J.; Intissar, M.; Ouvrard, G.; Nazar, L. F. *J. Mater. Chem.* **2002**, *12*, 3245−3253.
(15) Zampardi, G.; Ventosa, E.; La Mantia, F.; Schuhmann, W. *Chem. Commun.* **2013**, *49*, 9347−9349.
(16) Jacoby, M. *Chem. Eng. News* **2013**, *91*, 33−37.
(17) Armstrong, A. R.; Armstrong, G.; Canales, J.; García, R.; Bruce, P. G. *Adv. Mater.* **2005**, *17*, 862−865.
(18) Hu, Y.-S.; Kienle, L.; Guo, Y.-G.; Maier, J. *Adv. Mater.* **2006**, *18*, 1421−1426.
(19) Wang, K.; Wei, M.; Morris, M. A.; Zhou, H.; Holmes, J. D. *Adv. Mater.* **2007**, *19*, 3016−3020.
(20) Yang, Z.; Choi, D.; Kerisit, S.; Rosso, K. M.; Wang, D.; Zhang, J.; Graff, G.; Liu, J. *J. Power Sources* **2009**, *192*, 588−598.
(21) Ren, Y.; Hardwick, L. J.; Bruce, P. G. *Angew. Chem., Int. Ed.* **2010**, *49*, 2570−2574.
(22) Shin, J.-Y.; Samuelis, D.; Maier, J. *Adv. Funct. Mater.* **2011**, *21*, 3464−3472.
(23) Saravanan, K.; Ananthanarayanan, K.; Balava, P. *Energy Environ. Sci.* **2010**, *3*, 939−948.
(24) Szeifert, J. M.; Feckl, J. M.; Fattakhova-Rohlfing, D.; Liu, Y.; Kalousek, V.; Rathouský, J.; Bein, T. *J. Am. Chem. Soc.* **2010**, *132*, 12605−12611.
(25) Ren, Y.; Liu, Z.; Pourpoint, F.; Armstrong, A. R.; Grey, C. P.; Bruce, P. G. *Angew. Chem., Int. Ed.* **2012**, *51*, 2164−2167.
(26) Chen, S. C.; Tan, Y. L.; Li, C. M.; Cheah, Y. L.; Luan, D.; Madhavi, S.; Boey, F. Y. C.; Archer, L. A.; Lou, X. W. *J. Am. Chem. Soc.* **2010**, *132*, 6124−6130.
(27) Zhao, B.; Shao, Z. *J. Phys. Chem. C* **2012**, *116*, 17400−17447.
(28) Wang, J.; Polleux, J.; Lim, J.; Dunn, B. *J. Phys. Chem. C* **2007**, *111*, 14925−14931.
(29) Wagemaker, M.; Mulder, F. M. *Acc. Chem. Rev.* **2012**, *46*, 1206−1215.
(30) Bi, Z.; Paranthaman, M. P.; Guo, B.; Unocic, R.; Meyer, H.; Bridges, C. A.; Sun, X.-G.; Dai, S. *J. Mater. Chem. A* **2013**, DOI: 10.1039/C3TA14535B.
(31) Li, H.; Zhou, H. *Chem. Commun.* **2012**, *48*, 1201−1217.
(32) Guo, Y.-G.; Hu, Y.-S.; Sigle, W.; Maier, J. *Adv. Mater.* **2007**, *19*, 2087−2091.
(33) Ding, S.; Chen, J. S.; Lou, X. W. *Adv. Funct. Mater.* **2011**, *21*, 4120−4125.
(34) Chen, J. S.; Wang, Z.; Dong, X. C.; Chen, P.; Lou, X. W. *Nanoscale* **2011**, *3*, 2158−2161.
(35) Yu, S. X.; Yang, L. W.; Tian, Y.; Yang, P.; Jiang, F.; Hu, S. W.; Wei, X. L.; Zhong, J. X. *J. Mater. Chem. A* **2013**, *1*, 12750−12758.
(36) Yang, S.; Fang, X.; Müllen, K. *Adv. Mater.* **2011**, *23*, 3575−3579.
(37) Liu, R.; Ren, Y.; Shi, Y.; Zhang, F.; Zhang, L.; Tu, B.; Zhao, D. *Chem. Mater.* **2008**, *20*, 1140−1146.
(38) Das, S. K.; Bhattacharyya, A. J. *J. Electrochem. Soc.* **2011**, *158*, A705−A710.

(39) Liu, D.; Lei, J.-H.; Guo, L.-P.; Deng, K.-J. *Microporous Mesoporous Mater.* **2011**, *139*, 87−93.
(40) Wang, W.; Sa, Q.; Chen, J. S.; Wang, Y.; Jung, H.; Yin, Y. *ACS Appl. Mater. Interfaces* **2013**, *5*, 6478−6483.
(41) Petkovich, N. D.; Stein, A. *Chem. Soc. Rev.* **2013**, *42*, 3721−3739.
(42) Josephson, D. P.; Popczun, E. J.; Stein, A. *J. Phys. Chem. C* **2013**, *117*, 13585−13592.
(43) Meng, Y.; Gu, D.; Zhang, F.; Shi, Y.; Yang, H.; Li, Z.; Yu, C.; Tu, B.; Zhao, D. *Angew. Chem., Int. Ed.* **2005**, *44*, 7053−7059.
(44) Boettcher, S. W.; Bartl, M. H.; Hu, J. G.; Stucky, G. D. *J. Am. Chem. Soc.* **2005**, *127*, 9721−9730.
(45) Galusha, J. W.; Tsung, C. K.; Stucky, G. D.; Bartl, M. H. *Chem. Mater.* **2008**, *20*, 4925−4930.
(46) Schubert, U. *J. Mater. Chem.* **2005**, *15*, 3701−3715.
(47) Fattakhova-Rohlfing, D.; Wark, M.; Brezesinski, T.; Smarsly, B. M.; Rathouský, J. *Adv. Funct. Mater.* **2007**, *17*, 123−132.
(48) Procházka, J.; Kavan, L.; Shklover, V.; Zukalová, M.; Frank, O.; Kalbáč, M.; Zukal, A.; Pelouchová, H.; Janda, P.; Mocek, K.; Klementová, M.; Carbon, D. *Chem. Mater.* **2008**, *20*, 2985−2993.
(49) Chen, X.; Mao, S. S. *Chem. Rev.* **2007**, *107*, 2891−2959.
(50) Isley, S. L.; Penn, R. L. *J. Phys. Chem. C* **2008**, *112*, 4469−4474.
(51) Zhang, H.; Banfield, J. F. *J. Mater. Chem.* **1998**, *8*, 2073−2076.
(52) Ranade, M. R.; Navrotsky, A.; Zhang, H. Z.; Banfield, J. F.; Elder, S. H.; Zaban, A.; Borse, P. H.; Kulkarni, S. K.; Doran, G. S.; Whitfield, H. J. *Proc. Natl. Acad. Sci. U.S.A.* **2002**, *99*, 6476−6481.
(53) Huang, C.-H.; Gu, D.; Zhao, D.; Doong, R.-A. *Chem. Mater.* **2010**, *22*, 1760−1767.
(54) Cheng, P.-Y.; Huang, C.-H.; Doong, R.-A. *Carbon* **2012**, *50*, 4259−4268.
(55) Zhang, J.; Li, M.; Feng, Z.; Chen, J.; Li, C. *J. Phys. Chem. B* **2006**, *110*, 927−935.
(56) Hanaor, D. A. H.; Sorrell, C. C. *J. Mater. Sci.* **2011**, *46*, 855−874.
(57) Yu, T.; Deng, Y. H.; Wang, L.; Liu, R. L.; Zhang, L. J.; Zhao, D. *Adv. Mater.* **2007**, *19*, 2301−2306.
(58) Swamy, V.; Kuznetsov, A.; Dubrovinsky, L. S.; McMillan, P. F.; Prakapenka, V. B.; Shen, G.; Muddle, B. C. *Phys. Rev. Lett.* **2006**, *96*, 135702(1−4).
(59) Grey, I. E.; Li, C.; Madsen, I. C.; Braunshausen, G. *Mater. Res. Bull.* **1988**, *23*, 743−753.
(60) Balachandran, U.; Eror, N. G. *J. Solid State Chem.* **1982**, *42*, 276−282.
(61) Zhang, W. F.; He, Y. L.; Zhang, M. S.; Yin, Z.; Chen, Q. *J. Phys. D: Appl. Phys.* **2000**, *33*, 912−916.
(62) Ferrari, A. C.; Robertson, J. *Phys. Rev. B* **2000**, *61*, 14095−14107.
(63) Bücker, W. *J. Non-Cryst. Solids* **1973**, *12*, 115−128.
(64) Fierke, M. A. Ph.D. Thesis, University of Minnesota-Twin Cities, 2013.
(65) Ko, T.-H.; Kuo, W.-S.; Chang, Y.-H. *Polym. Composites* **2000**, *21*, 745−750.
(66) Meng, Y.; Gu, D.; Zhang, F.; Shi, Y.; Cheng, L.; Feng, D.; Wu, Z.; Chen, Z.; Wan, Y.; Stein, A.; Zhao, D. *Chem. Mater.* **2006**, *18*, 4447−4464.
(67) Errington, R. J.; Ridland, J.; Clegg, W.; Coxall, R. A.; Sherwood, J. M. *Polyhedron* **1998**, *17*, 659−674.
(68) Vu, A.; Stein, A. *Chem. Mater.* **2011**, *23*, 3237−3245.
(69) Zeng, L.; Zheng, C.; Xia, L.; Wang, Y.; Wei, M. *J. Mater. Chem. A* **2013**, *1*, 4293−4299.
(70) Jiang, H.; Yang, X.; Chen, C.; Zhu, Y.; Li, C. *New J. Chem.* **2013**, *37*, 1578−1583.
(71) Xin, X.; Zhou, X.; Wu, J.; Yao, X.; Liu, Z. *ACS Nano* **2012**, *6*, 11035−11043.
(72) Zhao, B.; Jiang, S.; Su, C.; Cai, R.; Ran, R.; Tadé, M. O.; Shao, Z. *J. Mater. Chem. A* **2013**, *1*, 12310−12320.
(73) Kubiak, P.; Geserick, J.; Hüsing, N.; Wohlfahrt-Mehrens, M. *J. Power Sources* **2008**, *175*, 510−516.
(74) Wang, D.; Choi, D.; Yang, Z.; Viswanathan, V. V.; Nie, Z.; Wang, C.; Song, Y.; Zhang, J.-G.; Liu, J. *Chem. Mater.* **2008**, *20*, 3435−3442.
(75) Liu, H.; Bi, Z.; Sun, X.-G.; Unocic, R. R.; Paranthaman, M. P.; Dai, S.; Brown, G. M. *Adv. Mater.* **2011**, *23*, 3450−3454.
(76) Myung, S.-T.; Takahashi, N.; Komaba, S.; Yoon, C. S.; Sun, Y.-K.; Amine, K.; Yashiro, H. *Adv. Funct. Mater.* **2011**, *21*, 3231−3241.
(77) Wang, J.; Zhou, Y.; Hu, Y.; O'Hayre, R.; Shao, Z. *J. Phys. Chem. C* **2011**, *115*, 2529−2536.
(78) Yoon, S.; Manthiram, A. *J. Phys. Chem. C* **2011**, *115*, 9410−9416.
(79) Zhou, Y.-K.; Cao, L.; Zhang, F.-B.; He, B.-L.; Li, H.-L. *J. Electrochem. Soc.* **2003**, *150*, A1246−A1249.
(80) Ho, C.; Raistrick, I. D.; Huggins, R. A. *J. Electrochem. Soc.* **1980**, *127*, 343−350.